The Astrophysical Journal, 950:168 (11pp), 2023 June 20 https://doi.org/10.3847/1538-4357/acd4ba

The Nonorthogonal X-line in a Small Guide-field Reconnection Event in the Magnetotail

Yi Qi[1], Robert Ergun[1], Neha Pathak[1], Tak Chu Li[2], Stefan Eriksson[1], Alexandros Chasapis[1], Steven J Schwartz[3], Narges Ahmadi[1], Tien Vo[1], David Newman[1], Maria Usanova[1], Frederick D Wilder[4], and Jason Shuster[5]
[1] Laboratory for Atmospheric and Space Physics, Boulder, CO, USA; yi.qi@lasp.colorado.edu
[2] Department of Physics and Astronomy, Dartmouth College, Hanover, NH, USA
[3] Imperial College London, London, UK
[4] University of Texas at Arlington, Arlington, TX, USA
[5] University of Maryland College Park, College Park, MD, USA
Received 2023 March 9; revised 2023 April 21; accepted 2023 May 10; published 2023 June 22

Abstract

Magnetic reconnection is a fundamental plasma process that has been studied with analytical theory, numerical simulations, in situ observations, and laboratory experiments for decades. The models that have been established to describe magnetic reconnection often assume a reconnection plane normal to the current sheet in which an antiparallel magnetic field annihilates. The annihilation points, also known as the X-points, form an *x*-line, which is believed to be perpendicular to the reconnection plane. Recently, a new study using Magnetospheric Multiscale mission observations has challenged our understanding of magnetic reconnection by providing evidence that the *x*-line is not necessarily orthogonal to the reconnection plane. In this study we report a second nonorthogonal *x*-line event with similar features as that in the previous case study, supporting that the sheared *x*-line phenomenon is not an aberrant event. We employ a detailed directional derivative analysis to identify the *x*-line direction and show that the in-plane reconnection characteristics are well maintained even with a nonorthogonal *x*-line. In addition, we find the *x*-line tends to follow the magnetic field on one side of the current sheet, which suggests an asymmetry across the current sheet. We discuss the possibility that the nonorthogonal *x*-line arises from an interplay between the two aspects of reconnection: the macroscopic magnetic field topology and microscopic particle kinetics.

Unified Astronomy Thesaurus concepts: Plasma physics (2089); Space plasmas (1544)

1. Introduction

Magnetic reconnection is a fundamental plasma process found in a multitude of plasma environments. Magnetic reconnection has been observed and studied in the heliosphere, for example, in the solar corona (Smartt et al. 1993; Xue et al. 2016), in the solar wind (Gosling et al. 2005; Fargette et al. 2020; Phan et al. 2020), near Earth in the turbulent shock transition region (Gingell et al. 2019; Wang et al. 2019), in the magnetosheath (Retinò et al. 2007; Eriksson et al. 2018; Phan et al. 2018), at the magnetopause (Burch et al. 2016; Ergun et al. 2017; Russell et al. 2017; Webster et al. 2018), as well as in magnetotail current sheets (Torbert et al. 2018; Rogers et al. 2019; Ergun et al. 2020; Hubbert et al. 2021). Magnetic reconnection is important not only because it is ubiquitous but also because it enables explosive energy conversion from fields to particles, which leads to significant heating and acceleration (Dahlin et al. 2014; Chen et al. 2016; Graham et al. 2016; Fujimoto & Cao 2021) and at the same time, modifies the magnetic field topology (Dungey 1961; Fu et al. 2019; Øieroset et al. 2019; Russell & Qi 2020; Qi et al. 2020; Jia et al. 2021). Being a multiscale process, magnetic reconnection occurs in a microscopic diffusion region but also has a macroscopic impact. To deepen our understanding of magnetic reconnection, it is crucial to establish an accurate and realistic picture of the diffusion region.

Many of the current models of magnetic reconnection, especially quasi-2D models, often are based on a reconnection plane in which an antiparallel magnetic field annihilates. The annihilation points, also known as the x-points, form an *x*-line, which in a quasi-2D model, is perpendicular to the reconnection plane (Parker 1957; Cassak & Shay 2007). Along the *x*-line, all reconnection planes are similar to each other. Thus, little variation would be expected along the *x*-line.

To describe magnetic reconnection, the right-handed LMN coordinate system is defined with L along the antiparallel magnetic field direction, N the normal of the reconnecting current sheet, and M the *x*-line direction. Thus, the $L-N$ plane is the reconnection plane.

In the reconnection plane, there are some distinguishable characteristics suggesting active reconnection in a current sheet. For example, the Alfvénic plasma outflow jets (Cassak & Shay 2007), the Hall magnetic and electric fields (Drake et al. 2008; Graham et al. 2016; Genestreti et al. 2020), and a thin electron current sheet (Chen et al. 2008). Near the *x*-line there is an enhanced energy conversion rate measured by $\boldsymbol{J}\cdot\boldsymbol{E}'$ where $\boldsymbol{J}$ is the current density and $\boldsymbol{E}'$ is the nonideal electric field ($\boldsymbol{E}'=\boldsymbol{E}+\boldsymbol{V_e}\times\boldsymbol{B}$. $\boldsymbol{E}$ is the electric field, $\boldsymbol{V_e}$ is the electron velocity, and $\boldsymbol{B}$ is the magnetic field) (Burch et al. 2018; Pritchard et al. 2019; Hesse & Cassak 2020; Lu et al. 2020). In addition, the velocity of the magnetic flux transport (U_ψ) has recently been proven to be a localized indicator of active reconnection (Li et al. 2021; Ng et al. 2022; Qi et al. 2022).

The quasi-2D picture provides us with a convenient basis for describing magnetic reconnection. Often, it successfully captures the essence of the reconnection and can explain some of the most important characteristics of this process.

Even though the quasi-2D picture is fairly well established and verified, it remains a challenge to fully understand the

three-dimensional (3D) behaviors of magnetic reconnection. Studies have focused on large-scale 3D behavior (Phan et al. 2001; Paschmann et al. 2013; Zou et al. 2019; Fuselier et al. 2021), patchy reconnections (Kan 1988; Genestreti et al. 2022), and the deflections of the x-line (Hesse et al. 2013; Liu et al. 2018). A recent study by Pathak et al. (2022) showed a fortuitous case in which the alignment of two MMS spacecraft and directional derivative analysis suggest that the direction of the x-line is not necessarily normal to the reconnection planes. Instead, the x-line, which we call the M' direction, appears to deviate from the M direction by approximately 40°–60° in the $L-M$ plane. In the case reported by Pathak et al. (2022), MMS has rapid ($\sim$250 km s^{-1}) apparent motion in the L direction relative to the x-line, while the ion retreat velocity (the measured ion velocity at the x-line) is much smaller, which could be explained by a sheared x-line. Apparent motion in the L direction can result from physical motion in the M direction if the x-line is sheared. However, in the reconnection plane, active reconnection signatures remain nearly the same as in the quasi-2D picture. This picture is different from the classic quasi-2D reconnection where the x-line is perpendicular to the reconnection plane and suggests that, while reconnection is still quasi-planar, the x-line direction can be nonorthogonal to the reconnection plane.

This paper is organized as follows. In Section 2, we review the context of a second such event, establish the LMN coordinates, and examine the reconnecting current sheet, where we show why an orthogonal x-line cannot explain some aspects of the observations. In Section 3, we investigate the interpretation of the directional derivative analysis to identify the x-line direction and present results that show a significant difference between the M' (the x-line direction) and the M direction. In Section 4 we show the in-plane reconnection features observed at all four spacecraft, which suggests even with a sheared x-line, reconnection can still be quasi-planar, and the in-plane characteristics are not significantly altered from a 2D picture. In Section 5, we discuss the possible uncertainty sources and potential causes of a nonorthogonal x-line. In Section 6, we summarize our discoveries.

2. Event Overview

A magnetic reconnection event observed on 2017 August 10 was first studied by Zhou et al. (2019). It is reported as an electron diffusion region (EDR) crossing in the magnetotail. MMS located at $\sim$[−15.2, 4.6, 3.0] Earth radii (R_E) in the Geocentric Solar Ecliptic (GSE) coordinate system. Figure 1 shows the context of this event from 12:17:30–12:19:50 UT as observed by MMS 2. The EDR crossing is at $\sim$12:18:34 UT. The data we use came from the fluxgate magnetometer (FGM; Russell et al. 2016), the double-probe electric field instrument (EDP; Ergun et al. 2016; Lindqvist et al. 2016; Torbert et al. 2016), and the fast plasma instrument (FPI; Pollock et al. 2016).

Panel (a) of Figure 1 plots the magnetic components and magnitude in GSE coordinates. The magnetic field is dominated by the x component, B_x. The reversal of B_x at $\sim$ 12:18:33 UT indicates that MMS crosses from the southern to the northern hemisphere. B_x reverses again after the event, which indicates the flapping motion of the magnetotail plasma sheet. Near the current sheet, the dominating electric field component E_z (the z component of the electric field, blue trace, Figure 1(b)) increases, and the peaks switch from positive to negative. The electron number density (n_e, Figure 1(c)) is about 0.15 cm^{-3} at the current sheet, yielding an electron inertial length (d_e) of $\sim$14 km, which is slightly smaller than the spacecraft separation ($\sim$21 km). Panels (d) and (e) show the ion velocity (V_i) and electron velocity (V_e). The fast ion flows are at the order of proton Alfvén speed V_A calculated by $V_A = B \cdot \sqrt{\mu_0 n_p m_p}^{-1}$, where B is the magnitude of the magnetic field, μ_0 is the vacuum permeability, n_p is the proton number density and m_p is the mass of a proton. If using $B \sim$ 10 nT, $n_p \sim n_e \sim 0.15$ cm^{-3}, the Alfvén speed is about 560 km s^{-1}. $V_{i,x}$, the x component of V_i, changes sign at the EDR current sheet, consistent with bidirectional ion outflows from the reconnection site. V_e has a prominent super-proton-Alfvénic peak at the current sheet, indicating the current is primarily carried by electrons. Panels (f) and (g) show the omnidirectional differential energy flux of ions and electrons. We see little change in the plasma's omnidirectional energy spectra at the magnetic reconnection site. Panels (h)–(j) show the electron pitch angle distributions of the low-energy range (10–200 eV), mid-energy range (200–2000 eV), and high-energy range (2000 eV–30 keV). At the EDR, low-energy electrons (panel (h)) switch from being parallel to the magnetic field to antiparallel due to the change in the magnetic field direction. For mid- and high-energy electrons (panels (i) and (j)) they remained field aligned (most flux is at close to 0° or 180°) but we see enhanced fluxes at the EDR and imbalanced parallel/antiparallel fluxes near the current. The context of this event is similar to most reported reconnection events in the magnetotail.

In Figure 2, we zoom in on the current sheet and examine the details of reconnection-related parameters from 12:18:25–12:18:40 UT in the LMN coordinates. The LMN coordinates are preliminarily defined by minimum variance analysis (MVA). We use MVA on the four-spacecraft-averaged magnetic field and assign the component with maximum variance as L_0. We then use MVA on the four-spacecraft-averaged electric field and assign the component with maximum variance direction as N_0. Minor adjustments ($\sim$5°) are made to orthogonalize the two axes to obtain $M_0 = N_0 \times L_0$. The adjustment finds the LMN directions that constrain the values of the B_M at each of the four spacecraft to be nearly identical at the B_L reversal point. This adjustment is based on the assumption that all four spacecraft measure the same guide field (B_g) strength at the current sheet crossing, $B_L = 0$. In this event, the guide field strength is about 1.9 nT (about $\sim$ 27% of the upstream reconnecting component $B_{L,\mathrm{up}} \sim 7$ nT), $L = [0.982, -0.131, -0.139]$, $M = [0.178, 0.888, 0.425]$, and $N = [0.067, -0.441, 0.894]$ in GSE. Our LMN directions differ from those used by Zhou et al. (2019) by about 10° (L), 5° (M), and 10° (N).

As discussed by Zhou et al. (2019), this event has clear EDR crossing signatures. Figures 2(a) and (b) demonstrate the magnetic field and electric field in the LMN coordinates. B_L reverses from negative to positive as does B_N. With a $B_g =$ 1.9 nT at the B_L reversal, B_M variation has positive-negative-positive signs which indicates a quadrupolar Hall magnetic field (see later). The electric field is dominated by the N component and has a bipolar signature at the current sheet, which is a characteristic of the Hall electric field. (There are fluctuations of E_N to the right of the current sheet which may be caused by drift waves or magnetic islands.) Panel (c) shows the current density calculated by $n_e q(\boldsymbol{V_i} - \boldsymbol{V_e})$, which has a strong peak in the M direction, consistent with the strong electron flow in the M (panel (f) green trace). The energy conversion $\boldsymbol{J} \cdot \boldsymbol{E}'$ is

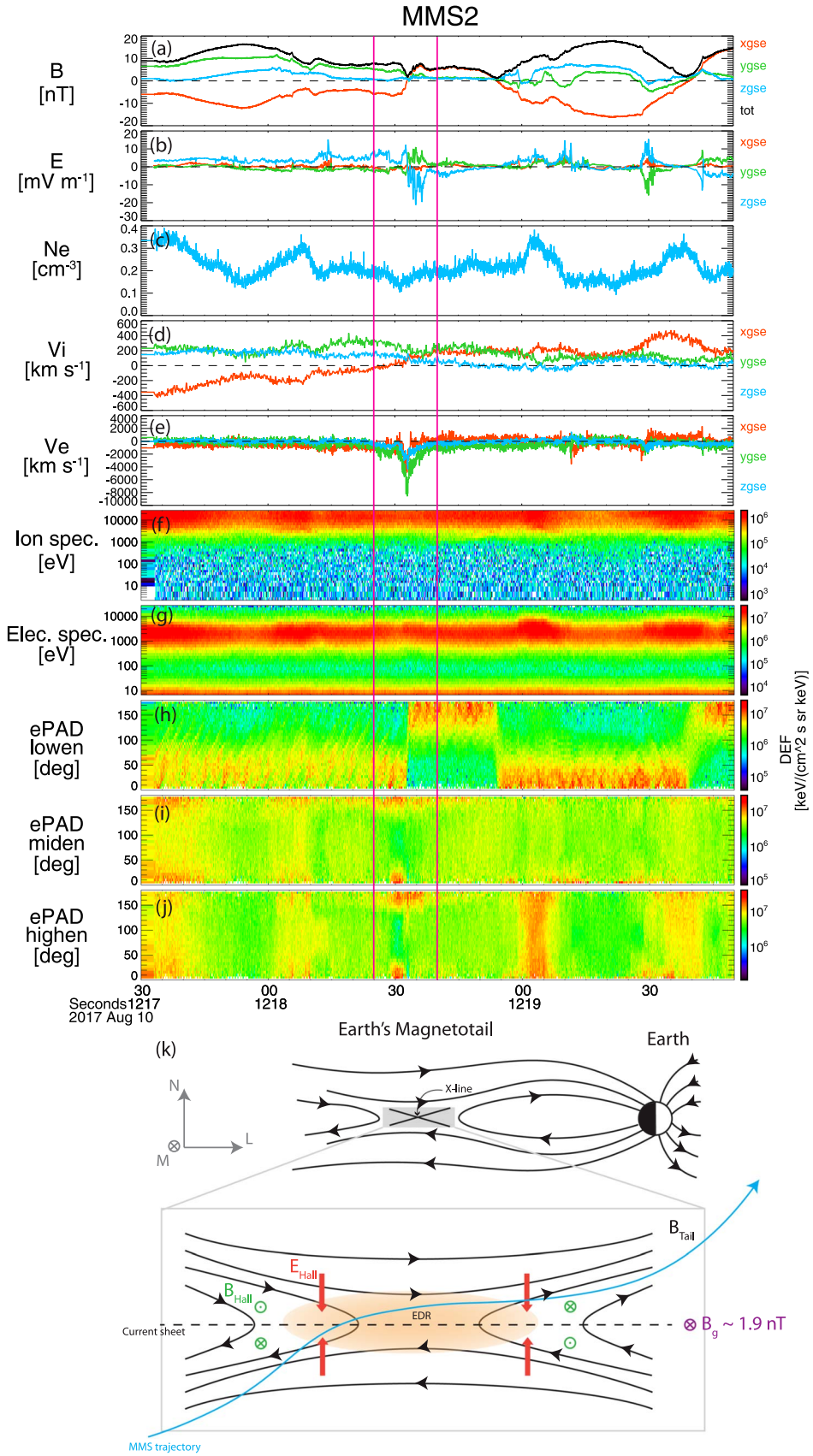

Figure 1. The context surrounding the EDR crossing observed by MMS2. (a) Magnetic field strength and components in GSE coordinates. (b) Electric field components in GSE coordinates. (c) Electron number density. (d), (e) The ion and electron velocity in GSE coordinates. (f), (g) Ion and electron omnidirectional differential energy flux. (h)–(j) The electron pitch angle distribution of the low-energy range (10–300 eV), mid-energy range (300–3000 eV), and high-energy range (3–30 keV). The vertical magenta lines highlight the EDR crossing event. (k) A schematic showing the context of Earth's magnetotail and the MMS trajectory in the vicinity of the EDR.

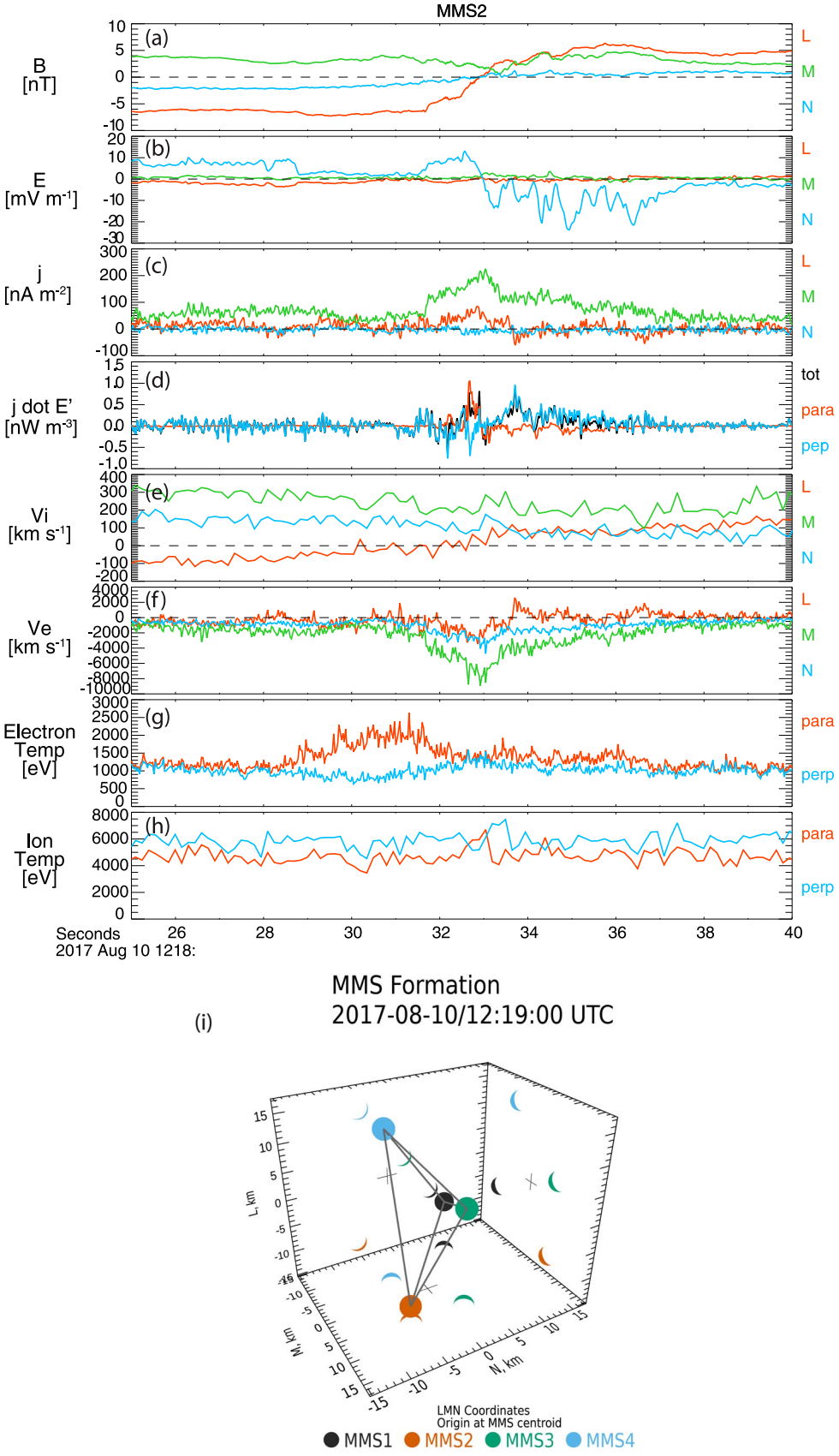

Figure 2. A magnified view of the EDR crossing event. (a) Magnetic field components in LMN. (b) Electric field components in LMN. (c) Current density in LMN. (d) Energy conversion rate $\boldsymbol{j} \cdot \boldsymbol{E}'$ where $\boldsymbol{j}$ is the current density and $\boldsymbol{E}' = \boldsymbol{E} + \boldsymbol{V}_e \times \boldsymbol{B}$, is the nonideal electric field. (e)–(f) Ion and electron velocity in LMN. (g)–(h) Electron and ion temperature parallel and perpendicular to the magnetic field. (i) MMS configuration in LMN.

positive at the current sheet. The ion and electron velocities (panels (e) and (f)) both reverse from negative L to positive L, which is expected as bidirectional plasma outflows leave the x-line. Ion and electron temperatures also increase as shown in panels (g) and (h) indicating energization. Panel (i) is the satellites' configuration in the LMN coordinates. MMS1 leads in the N direction, followed by MMS3, MMS4, and MMS2. The separation between MMS2 and MMS4 is small in the N direction, but these two are well separated in both L and M.

Even though this event has many of the expected quasi-2D reconnection signatures, there are some abnormal features. From Ampere's law, we can estimate how fast the EDR moves in the L direction relative to MMS using the current density normal component J_N and ΔB_M ($J_N \sim \frac{\Delta B_M}{\mu_0 \Delta L}$). Consider a 1 s interval around the B_L reversal, ΔB_M is about 3 nT and J_N is about 10 nA m^{-2}. Thus, the relative velocity in L should be on the order of 240 km s^{-1}, which is similar to what has been observed in other tail reconnection events where this relative velocity or the ion retreat speed is often a few hundreds of km s^{-1} and typically evident in the ion velocity. For example, the event reported by Ergun et al. (2022) has an ion retreat velocity of about -200 km s^{-1} and that reported by Torbert et al. (2018) has a retreat velocity of ~ -170 km s^{-1}, suggesting that our estimation of the velocity in L is reasonable. However, in this case, the actual ion velocity in the L direction at the current sheet crossing is very low and is positive, which is in the opposite direction of the structure's anti-sunward motion suggested by the negative to positive outflow jets as well as the velocity calculated by the spatiotemporal difference method (Shi et al. 2019; Hasegawa et al. 2022). Meanwhile, there is significant ion speed in the M direction, much higher than that in the L direction. The question arises: Why do the magnetic field observations suggest fast motion in L, while there is almost zero ion retreat velocity?.

Pathak et al. (2022) explain a similar phenomenon with a nonorthogonal x-line model, i.e., when reconnection planes are sheared, and the x-line is no longer perpendicular to the reconnection plane, but is along M'. If the spacecraft physically move in the M direction relative to the EDR, its location in L will also change. Thus, there can be apparent motion in L even though there is no actual motion. To investigate this possibility further, we apply directional derivative analysis to the magnetic field and to determine if this event may have a nonorthogonal x-line.

3. Directional Derivative Analysis and the Orientation of the X-line

The directional derivative of the magnetic field can be calculated following

$$\boldsymbol{D} = \boldsymbol{n} \cdot \nabla \boldsymbol{B}, \tag{1}$$

where $\boldsymbol{n}$ is a unit vector. If $\boldsymbol{n}$ is along an invariant direction, the directional derivative D is equal to zero. To determine $\boldsymbol{n}$ with the smallest directional derivative, Shi et al. (2005, 2019) developed a method called the minimum directional derivative (MDD), which solves the eigenvalue problem $(\boldsymbol{L} - \lambda \boldsymbol{I}) = 0$, where $\boldsymbol{L} = (\nabla \boldsymbol{B})(\nabla \boldsymbol{B})^T$ (T denotes transposition). The three eigenvalues λ_1, λ_2, and λ_3 represent the maximum, intermediate, and minimum values of $|\boldsymbol{D}|^2$, and the eigenvector that corresponds to the minimum eigenvalue represents the direction along which the directional derivative of the magnetic field is the smallest.

We, however, use a different computational approach to obtain a complete map of the directional derivative values within one hemisphere in GSE (the values of any two hemispheres are symmetric about the origin point) as Pathak et al. (2022) did in their study. This method employs a 126 (in latitude θ) by 500 (in longitude φ) array of $\boldsymbol{n}$ vectors to cover the hemisphere. The $\boldsymbol{n}$ vector in GSE Cartesian coordinate system can be expressed as $\boldsymbol{n} = [\cos\theta \cos\varphi, \cos\theta \sin\varphi, \sin\theta]$. Then in GSE coordinates where the positions of the four spacecraft can be easily found, we calculate the directional derivative of the magnetic field following the standard four-spacecraft gradient method (Dunlop et al. 1988) and average its absolute value over the time series: $\boldsymbol{D}(\boldsymbol{n}) = \boldsymbol{D}(\theta, \varphi) = \langle |\boldsymbol{n} \cdot \nabla \boldsymbol{B_i}| \rangle$ or $\boldsymbol{D}(\boldsymbol{n}) = \boldsymbol{D}(\theta, \varphi) = \langle |\boldsymbol{n} \cdot \nabla \boldsymbol{B}| \rangle$, where $\boldsymbol{B_i}$ is a component of the magnetic field ($\boldsymbol{i} = \boldsymbol{x}, \boldsymbol{y}, \boldsymbol{z}$ in GSE or $\boldsymbol{i} = \boldsymbol{l}, \boldsymbol{m}, \boldsymbol{n}$ in LMN). We note that in this study, the calculation is carried out in GSE Cartesian coordinates. The results then are displayed in a spherical coordinates map using latitude and longitude.

Figure 3 gives the directional derivative maps (in GSE) of magnetic field components and the magnetic field vector. For each map, the x-axis represents the GSE longitude, and the y-axis represents the GSE latitude. The color represents the value of the directional derivative. The deepest blue area points out the direction along which the directional derivative is the minimum, i.e., the M' direction.

Before calculating the derivatives of $\boldsymbol{B}$, we apply a low-pass filter (<0.25 Hz) to diminish the impact of wave fluctuations. The choice of the frequency range considers the length of the time interval and the local plasma conditions (which determine the waves' frequencies). Thus, the filter frequency range may need adjustment for a different event.

Filtering is important for acquiring an accurate minimum directional derivative. Table 1 shows the results of directional derivative analyses with filtered/unfiltered $\boldsymbol{B}$ vectors and components in both LMN and GSE coordinates. The ratios of the absolute values of the directional derivatives are used to estimate the quality of the diagnoses of M'. After locating the maximum and minimum values, the third (intermediate) direction is defined by the cross product of the minimum and maximum directions, and the directional derivative along this direction gives the intermediate directional derivative value. A large ratio of the intermediate to minimum direction derivative (the *value ratios* as listed in Table 1) is expected to yield a more accurate minimum directional derivative. The minimum directional derivative direction, M', remains unchanged whether we base this analysis on GSE or LMN, which is expected and manifests the robustness of the method. In our case, the difference in M' between filtered and unfiltered data is about 10°–20°. These differences can become larger in cases that have stronger wave activity.

Table 1 reveals several features of the directional derivative analysis. It is clear that applying a low-pass filter yields better value ratios and thus more accurate directions than using the raw data. The M' directions vary when applying the directional derivative analysis to different magnetic field components as scalars. These differences are expected as some components may have more than one *invariant* direction. For example, B_L is expected to change only in the N direction, so it should have a degenerate

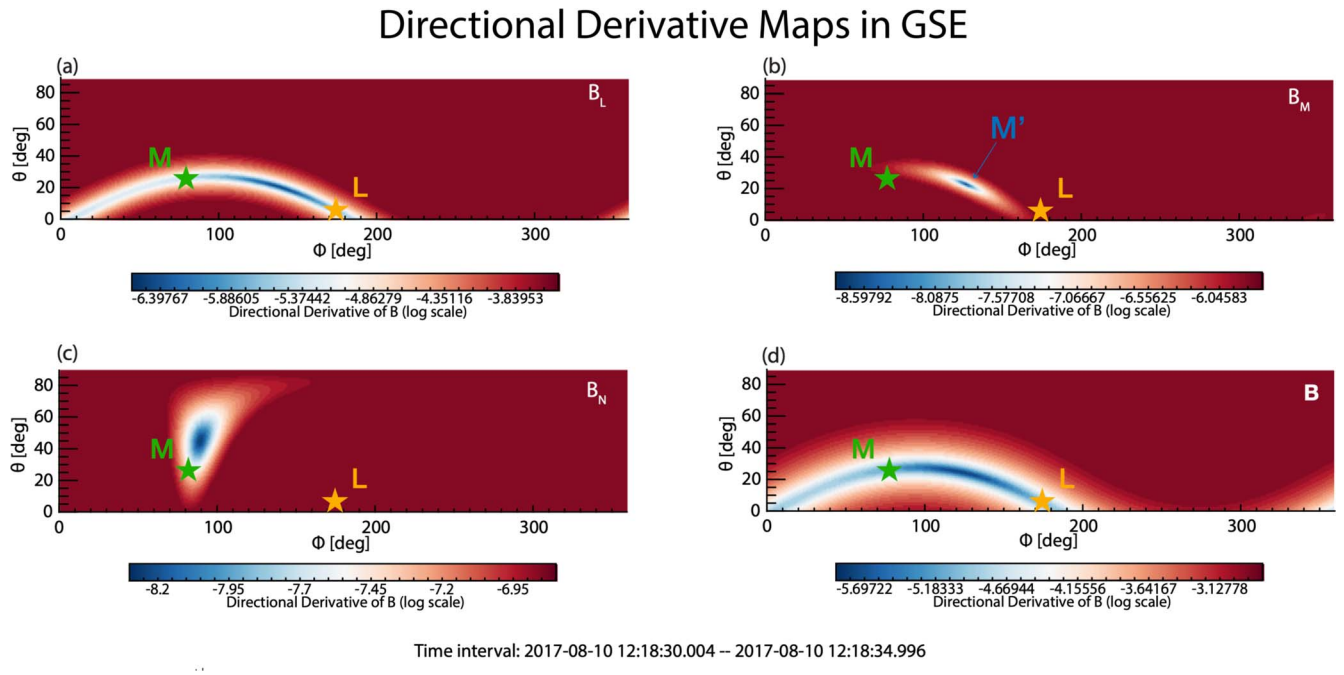

Figure 3. Directional derivative maps of a hemisphere in GSE. Directional derivative analysis using (a) the L component of the magnetic field. (b) the M component of the magnetic field. (c) the N component of the magnetic field. (d) the magnetic field vector in GSE. For each map, the x-axis is the longitude, and the y-axis is the latitude in degree. The color represents the value of the directional derivative results in log scale.

Table 1
Directional Derivative Results Before and After Filtering $\boldsymbol{B}$

	$\boldsymbol{B}$ in GSE: No Filter		$\boldsymbol{B}$ in GSE: 0.25 Hz Low-pass Filter		$\boldsymbol{B}$ in LMN: No Filter		$\boldsymbol{B}$ in LMN: 0.25 Hz Low-pass Filter	
	M to M' Angle	Value Ratio	M to M' Angle	Value Ratio	M to M' Angle	Value Ratio	M to M' Angle	Value Ratio
Vector	50.°4	1.97	38.°8	2.73	50.°4	1.97	38.°8	2.73
x; L	58.°1	2.50	55.°3	3.99	55.°3	2.40	52.°5	3.69
y; M	52.°3	1.75	30.°8	6.49	54.°2	2.07	42.°9	22.21
z; N	45.°8	1.27	6.°9	5.60	21.°3	2.22	21.°0	4.81

minimum directional derivative. B_N is expected to change in L, but since $|B_N| < |B_M|$, $|B_L|$ small measurement errors or errors in direction make its MDD less accurate. However, B_M is expected to have significant changes in both L and N. Thus, using B_M, we have the most confined minimum directional derivative area (panel (b) in Figure 3), with the largest mid/min value ratio among all components and vector results (filtered data). This suggests that, by using B_M, we can obtain the best-defined minimum directional derivative direction M', and as indicated in the last row of Table 1, the M' direction ($\sim$ [−0.54, 0.74, 0.40] in GSE) differs from M by about 40°. Considering the range of values in Table 1 and using the value ratio as a measure of accuracy, we estimate the uncertainty to be less than 14° (conservatively, the standard deviation of the M to M' angles from Table 1 weighted by the mid/min value ratio). Therefore, the 40° angle between M and M' is significant.

Recall the mysterious fast motion in L ($\sim$240 km s^{-1}) while there is no ion retreat velocity along L. We proposed earlier to explain this by the apparent motion caused by the nonorthogonal x-line. Now we verify this hypothesis with the 40° difference between M' and M.

4. In-plane Magnetic Reconnection Features

Even though in this event the x-line is nonorthogonal, and the reconnection planes are sheared, the quasi-2D picture of reconnection in the L–N plane is well maintained. We plot several parameters in Figure 4 to demonstrate this feature.

Figure 4 shows the four-spacecraft trajectories in the $\boldsymbol{L}$–$\boldsymbol{N}$ plane. The $\boldsymbol{L} = \boldsymbol{0}$ point occurs when MMS1 observes the quantity $\boldsymbol{B_M} - \boldsymbol{B_g}$ to change sign, and the $\boldsymbol{N} = \boldsymbol{0}$ point occurs at the MMS1 $\boldsymbol{B_L}$ reversal. To convert the time series to distance, the position in $\boldsymbol{N}$ is estimated point-by-point following Ampere's law in a similar way as described in Section 2: Starting from $\boldsymbol{J_M} \sim \partial \boldsymbol{B_L}/\partial \boldsymbol{N} - \partial \boldsymbol{B_N}/\partial \boldsymbol{L}$, $\Delta \boldsymbol{N}$ can be written as $\Delta \boldsymbol{N} \sim \Delta \boldsymbol{B_L}/(\boldsymbol{J_M} + \langle \partial \boldsymbol{B_N}/\partial \boldsymbol{L} \rangle)$. As shown in Figure 2(a), the slope of $\boldsymbol{B_N}$ is small and nearly constant, which suggests a smooth progression in $\boldsymbol{L}$. Thus, the quantity $\partial \boldsymbol{B_N}/\partial \boldsymbol{L}$ can be treated as a small constant $\langle \partial \boldsymbol{B_N}/\partial \boldsymbol{L} \rangle$, which is a second-order correction that can be ignored for the $\boldsymbol{N}$ position estimation here.

The position in L is very difficult to calculate precisely, so we set the apparent velocity in $\boldsymbol{L}$ to be a constant value of 200 km s^{-1}. There are several ways to estimate the L motion. In Section 2, we estimated the $\boldsymbol{L}$ motion velocity to be $\sim$240 km s^{-1}

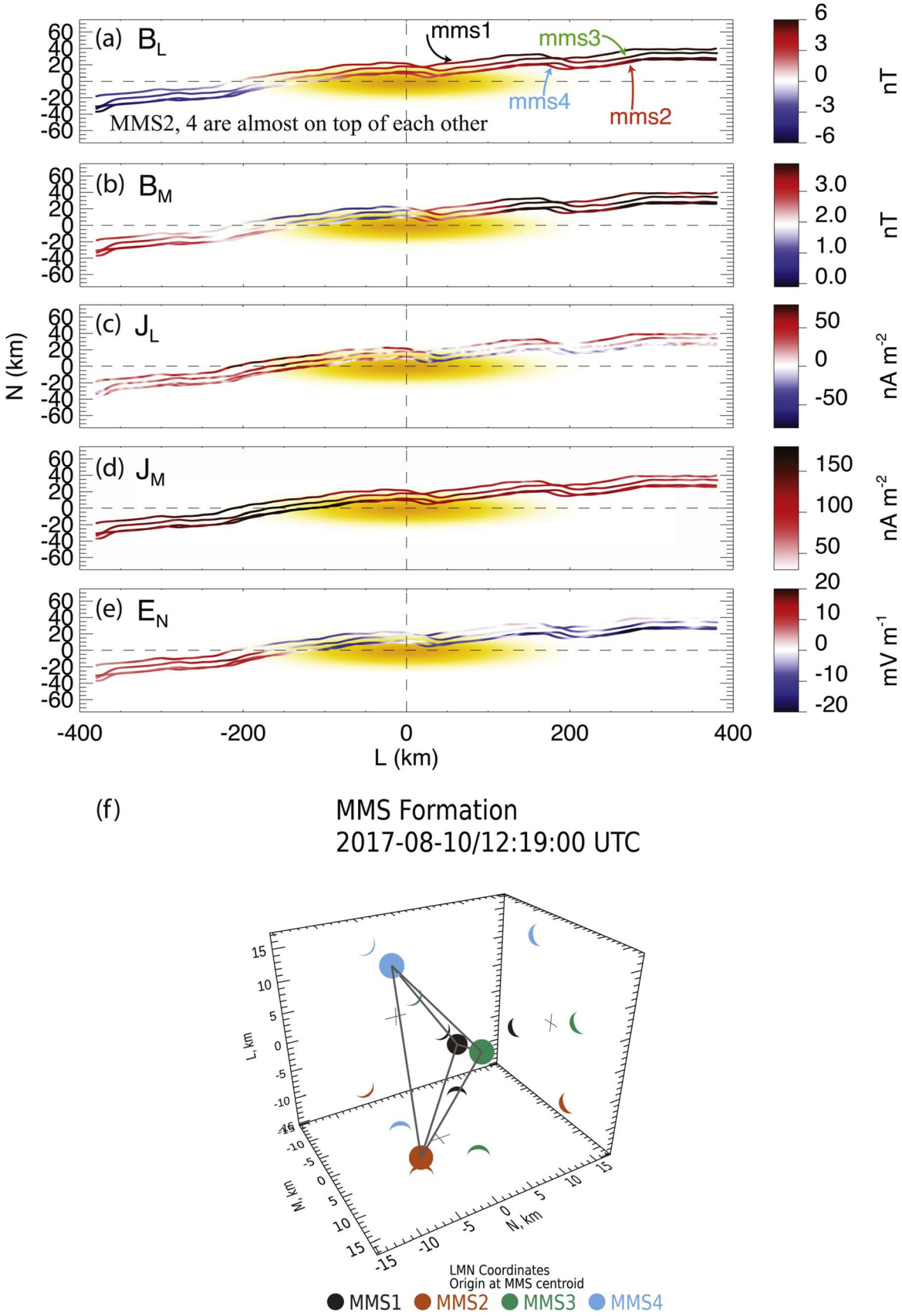

Figure 4. Trace plots: the measurements along the four MMS spacecraft trajectories in the L–N plane. (a) The magnetic field L component. (b) The magnetic M component. (c) The current density L component. (d) The current density M component. (e) The electric field N component. (f) The configuration of the MMS spacecraft. For each trace plot, the x-axis is the distance in L, and the y-axis is the distance in N. The yellow area in each panel represents the estimated location of the EDR.

in the vicinity of the x-line using $\Delta \boldsymbol{B_M}$ and $\boldsymbol{J_N}$. However, this calculation cannot be repeated point by point because the variation in $\boldsymbol{B_M}$ is negligible further away from the x-line (Figure 2 Panel (a)). We also can estimate the L motion velocity by the time span of the outflow jets' reversals. For ions, if we assume the jets reverse in about 10 ion skin depths $\boldsymbol{d_i}$ ($\boldsymbol{d_i} \sim 43\boldsymbol{d_e} \sim 600$ km) over $\sim$20 s (Figure 1(d)) we have a $\boldsymbol{L}$ velocity of $\sim$300 km s^{-1}. For electrons, if the jets reverse in about 10 electron skin depths over 1 s (Figure 2(f)), the L velocity is $\sim$ 150 km s^{-1}. We choose the L velocity to be 200 km s^{-1} as a combined estimate from the different approaches. We also note the $\boldsymbol{L}$ velocity has an uncertainty of $\sim$50%. However, this uncertainty is not critical to the conclusions as the $\boldsymbol{L}$ velocity may change the appearance of the trace plots (stretching or squeezing traces in $\boldsymbol{L}$) but does not dramatically change the physics behind it (see Pathak et al. 2022 for details).

Each panel of Figure 4 contains four traces representing the four spacecraft. From top to bottom, the four traces are MMS1, MMS3, MMS4, and MMS2. The colors of the traces represent the values of the parameters measured by the spacecraft. For all spacecraft, B_L and E_N reverse at $N = 0$, which is the current sheet crossing (panels (a) and (e)). In panel (d), J_M is intense around $N = 0$, also consistent with the current sheet crossing. With a 1.9 nT guide field removed, B_M variation shows the expected quadrupolar Hall-field signature (panel (b)). J_L has a strong jet on one side, which is expected because the reconnecting current sheet is very thin. On the right-hand side of EDR, the MMS spacecraft are moving above the current sheet and thus observe a less clear J_L jet (panel (c)).

Near $L = 0$, B_M–B_g and J_L both change signs. However, the reversal points of the magnetic field and the current density do not exactly colocate. A possible reason is due to the nonorthogonal x-line. Following Ampere's law

$$J_L = \frac{1}{\mu_o}\left(\frac{\partial B_N}{\partial M} - \frac{\partial B_M}{\partial N}\right). \tag{2}$$

One can see that there is only one contributing term to J_L in orthogonal magnetic reconnection ($\partial B_M/\partial N$). However, with a sufficiently large angle between M and M' (θ), $\partial B_N/\partial M$ can be nonzero. Because $|B_N|$ is small and is expected to vary slowly with L, this term can make only a small contribution. However, if θ is as large as 40°, the variation along M can cause an observable change in the behavior of $\boldsymbol{B}$ and $\boldsymbol{J}$ in the L–N plane. One can quantify the contribution of $\partial B_N/\partial M$ by considering the transformation

$$\boldsymbol{M} = \boldsymbol{M'}\cos\theta + \boldsymbol{L'}\sin\theta \quad \boldsymbol{L} = \boldsymbol{L'}\cos\theta - \boldsymbol{M'}\sin\theta. \tag{3}$$

L' is perpendicular to M' and deviates from L by θ. Because

$$\begin{aligned}\frac{\partial B_N}{\partial M'} &= \frac{\partial B_N}{\partial M}\frac{\partial M}{\partial M'} + \frac{\partial B_N}{\partial L}\frac{\partial L}{\partial M'} \\ &= \frac{\partial B_N}{\partial M}\cos\theta - \frac{\partial B_N}{\partial L}\sin\theta = 0,\end{aligned} \tag{4}$$

one can estimate that in a nonorthogonal system

$$\frac{\partial B_N}{\partial M} = \tan\theta\,\frac{\partial B_N}{\partial L}. \tag{5}$$

In Figure 2(a) (blue trace), one can see that $\partial B_N/\partial L$ has a nearly constant but small positive contribution. As a result, J_L has a small positive offset, which is in consort with the small delay between the B_M reversal and J_L reversal seen in Figures 4(b) and (c).

Through examination of J_M and J_N using Ampere's law in the same fashion, we conclude that the in-plane behavior of $\boldsymbol{J}$ and $\boldsymbol{B}$ is not drastically altered in a nonorthogonal system. As shown above, J_L receives a small offset. J_M is largely unchanged. The contribution to J_N by $\partial B_L/\partial M$ is also small since B_L primarily varies with N. Interestingly, the changes in the in-plane behavior of $\boldsymbol{J}$ and $\boldsymbol{B}$ are expected to be nearly undetectable (by MMS) with small θ.

Unlike the quasi-2D picture, $\partial B_M/\partial M$ does not necessarily vanish in a nonorthogonal system. On the contrary, it is expected to be finite. Because $\nabla \cdot \boldsymbol{B} = 0$, if $\partial B_M/\partial M \neq 0$ then $\partial B_L/\partial L + \partial B_N/\partial N \neq 0$. This introduces asymmetry in L and/or N that may impact the microscopic physics of magnetic reconnection. A nonorthogonal system cannot be symmetric.

We notice the traces of MMS2 and MMS4, which are the bottom two in each of the panels in Figure 4, are very close to each other even though their locations differ significantly in both L and M (panel (f)). The possible reason is that the separation vector between MMS2 and MMS4 differs about $\sim$20° from M' (65° from M), which means MMS2 and MMS4 are separated nearly along the x-line. Under this condition, we expect the signatures observed by these two spacecraft have less variations than if the x-line orientation is along the orthogonal M direction. Furthermore, Figure 4 suggests that they pass close to the x-line. In Figure 5, we show supporting evidence using the magnetic flux transport (MFT) analysis (Li et al. 2021; Qi et al. 2022).

Panel (c) of Figure 5 shows the velocity of MFT ($V_{\rm MFT}$), which has been known to increase sharply around the x-line and decrease rapidly moving away from the x-line (Li et al. 2021, 2023; Ng et al. 2022; Qi et al. 2022). In panel (c), all four-spacecraft measure greatly enhanced $V_{\rm MFT}$, consistent with being an EDR crossing. The peak in $V_{\rm MFT}$ is much higher at MMS2 and MMS4 compared to the value of MMS1 and MMS3, indicating these two spacecraft are closer to the x-line.

5. Discussion

In this study, we perform a directional derivative on the magnetic field to determine the x-line direction. We note there are several conditions under which the accuracy of this method is compromised. In Section 3, we mentioned the wave activity at the current sheet crossing may affect the results of the minimum directional derivative, so it is important to apply a low-pass filter to diminish the influence of wave perturbations. It is equally important to choose the filter frequency based on the plasma conditions and the time span of the current sheet crossing. The ideal filter frequency should be low enough so that waves with frequencies as low as 1/2 of the lower hybrid frequency, ω_{lh} are eliminated ($\omega_{lh} = [(\Omega_i\Omega_e)^{-1} + \omega_{pi}^{-2}]^{-1/2}$, where Ω_i and Ω_e are the ion and electron cyclotron frequency, and ω_{pi} is the plasma frequency) (Ergun et al. 2017; Graham et al. 2019; Wang et al. 2022). At the same time, the low-pass frequency should not be smaller than the inverse of the current sheet time span. Another situation that requires using a directional derivative with caution is if the spacecraft separation is much larger than the electron inertial length. Because the spatial gradient calculation uses four spacecraft measurements and assumes the gradients are linear, changes at electron scales smaller than the spacecraft separation may not be correctly evaluated.

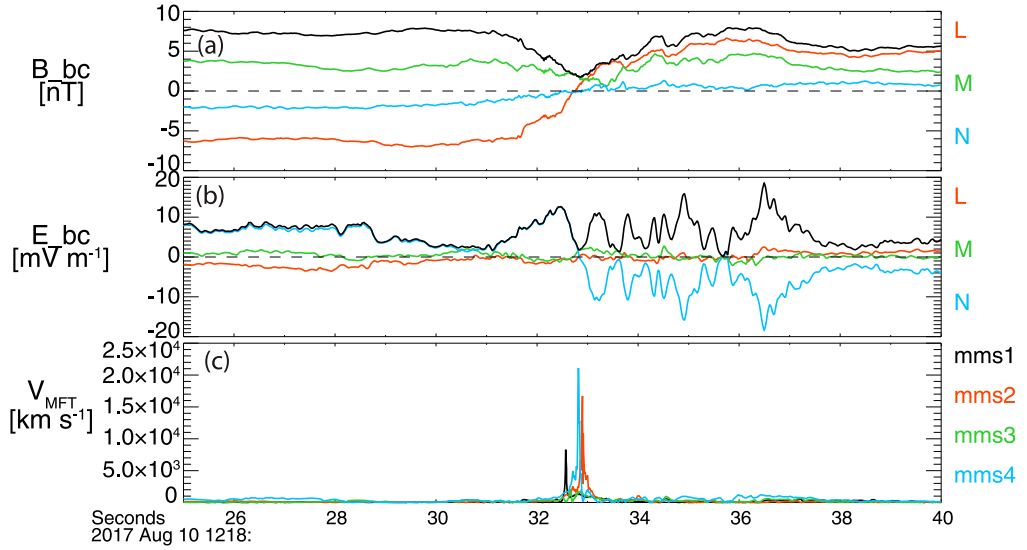

Figure 5. The electric field and magnetic field flux transportation at the EDR. (a), (b) the magnitude and components of the magnetic field and electric field in LMN. (c) The velocity of magnetic flux transportation.

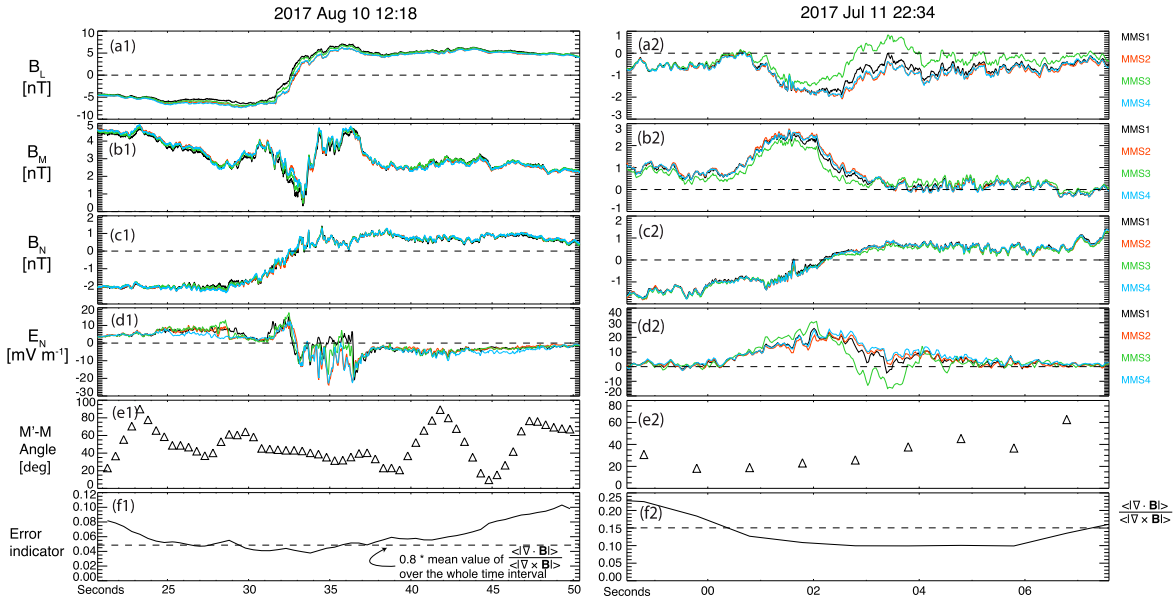

Figure 6. Running window of directional derivative analysis with the error indicator for two events. (a1, a2)–(c1, c2) magnetic field *L*, *M*, and *N* component of MMS1–4. (d1, d2) Electric *N* component of MMS1–4. (e1, e2) the angle between M' and M in each running window. (f1, 2) the error indicator $|\nabla \cdot \mathrm{B}|/|\nabla \times \mathrm{B}|$.

The quality of the directional derivative measurement can be revealed by the measured ratio of $\langle|\nabla \cdot \boldsymbol{B}|/|\nabla \times \boldsymbol{B}|\rangle$ (Shi et al. 2019; Hasegawa et al. 2022). The average measured value of $\langle|\nabla \cdot \boldsymbol{B}|\rangle$ indicates the lower limit of a directional derivative of $\boldsymbol{B}$ while $\langle|\nabla \times \boldsymbol{B}|\rangle$ indicates its magnitude. A small ratio indicates good measurement quality. Figure 6(f1) displays this quality indicator in a running window of 5 s with a step length of 0.5 s, and the angle between M' and M is plotted from each window (panel (e1)). Panels (a1)–(d1) of Figure 6 show the magnetic and electric field components of the event. Near the current sheet crossing and EDR, the $|\nabla \cdot \boldsymbol{B}|/|\nabla \times \boldsymbol{B}|$ is relatively low. In this region, the M'–M angle remains relatively constant at around 40° compared to the rest of the interval. Outside of the EDR and away from the current sheet, the directional derivative varies and may not represent the characteristics of the *x*-line.

In addition to the Aug 10 event, we show another event on 2017 July 11 reported by Torbert et al. (2018). In contrast to the Aug 10 event, the July 11 event has a much smaller angle between M' and M. The right-hand side of Figure 6 has the same format as the left-hand side. The EDR crossing is around 22:34:02–22:34:03. During this interval, the difference between M' and M is about 20°, which is much less significant and can possibly fall into the uncertainty range of the LMN coordinates determination (e.g., Denton et al. 2018; Genestreti et al. 2018). Thus, we cannot identify the July 11 event as a nonorthogonal *x*-line event. These two events are both in the magnetotail and MMS observed similar reconnection signatures. The orientation of the *x*-line is one of the major differences, which raises the question: What determines the *x*-line to be orthogonal or nonorthogonal?

There are several mechanisms that may result in a nonorthogonal system (see Pathak et al. 2022). Large-scale forcing is one possibility. Our analysis shows that a small angle between M and M' has little effect on the in-plane behavior of

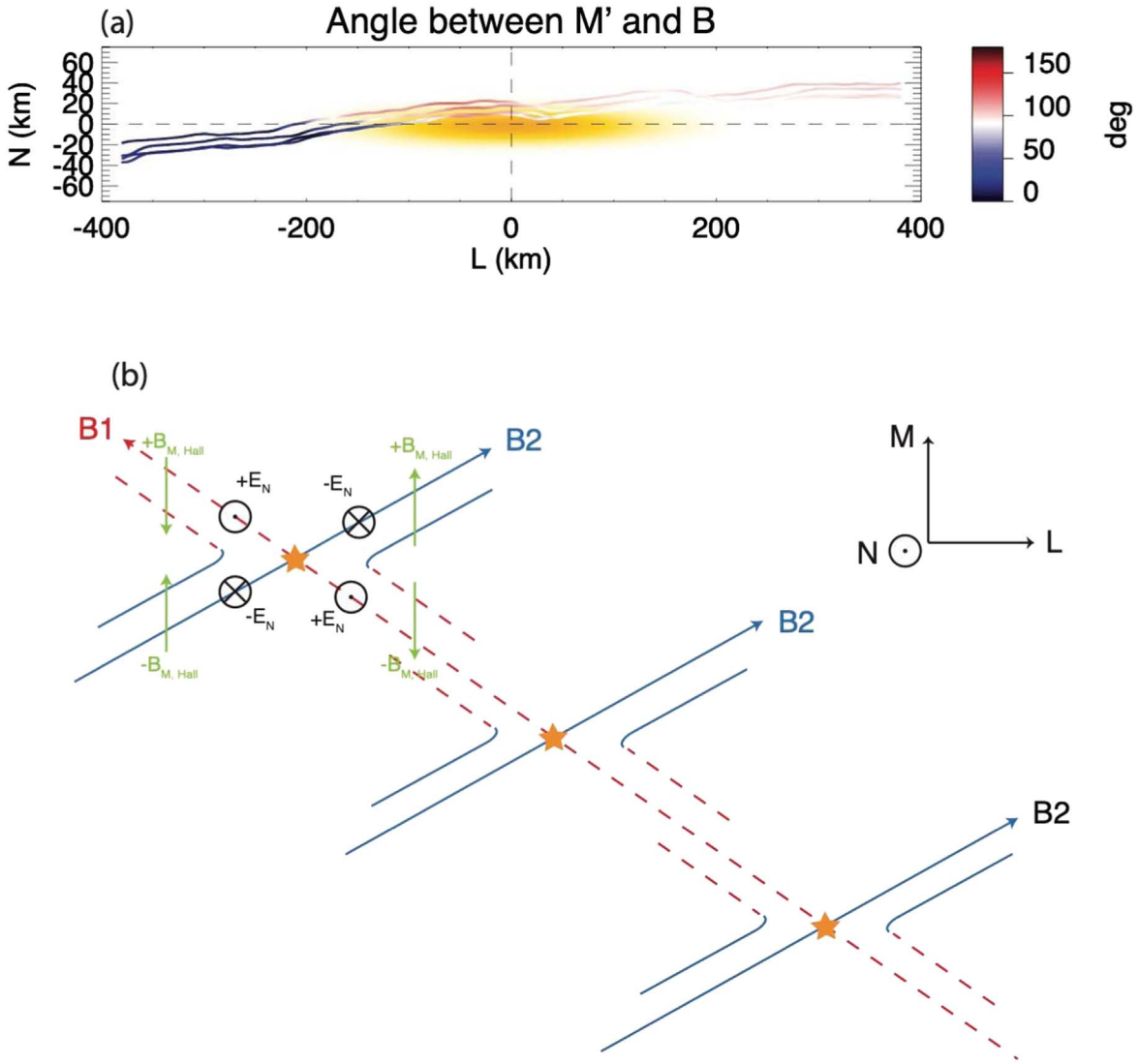

Figure 7. The angle between the M' direction and the magnetic field. (a) A trace plot in the $L-N$ plane showing the angles between M' and the magnetic field on four spacecraft. The format is the same as the trace plots in Figure 4. (b) A sketch demonstrating the field geometry in the $L-M$ plane. The $L-M$ plane contains the current sheet, and $\boldsymbol{B_1}$ is behind the plane while $\boldsymbol{B_2}$ is in front of the plane. The black circles represent the Hall electric field along N, and the green arrows represent the Hall magnetic field along M. The yellow star marks the reconnection sites. The continuous reconnection sites make up a nonorthogonal x-line that is more parallel to $\boldsymbol{B_1}$ but has a larger angle between $\boldsymbol{B_2}$. Note the drawing is not to scale.

$\boldsymbol{B}$ and $\boldsymbol{J}$, which suggests that there is no strong theoretical preference (in electron physics) for an orthogonal x-line. On the other hand, a nonorthogonal system must be asymmetric to ensure $\nabla \cdot \boldsymbol{B} = 0$, which opens the possibility that an asymmetry may govern the orientation of the x-line.

Another possibility is that MMS encountered an evolving magnetic reconnection event, for example, a spreading x-line. The speed of the x-line spreading is suggested to be the faster of the current carrier's speed and the Alfvén speed corresponding to the guide field strength (Huba & Rudakov 2002; Schreier et al. 2010; Shepherd & Cassak 2012), and also shown to depend on the thickness of the current sheet (Li et al. 2020). In a more recent study, the two mechanisms are unified by using the gradient of electric field L component along M at the boundary between reconnecting and non-reconnecting area (Arencibia et al. 2021). As for the orientation of the x-line, it is suggested to be the direction that maximizes the outflow speed from the x-line (given by an appropriately defined Alfvén speed) (Swisdak & Drake 2007), maximizes the reconnection rate (Schreier et al. 2010; Liu et al. 2018), minimize the in-plane current (Gonzalez et al. 2016), or maximize the oblique tearing growth rate (Liu et al. 2015). The existence of the guide field introduces asymmetry to the system and adds the complexity. In the presence of a guide field, it is suggested that x-lines do not take on a single orientation but instead exhibit a distribution of orientations (e.g., Schreier et al. 2010).

One interesting feature that we find in the August 10 event and in the event of Pathak et al. (2022) is that the x-line follows the magnetic field direction on one side of the current sheet and has a much larger angle to $\boldsymbol{B}$ on the other side as shown by Figure 7(a), which plots the angle between the M' direction and the local magnetic field direction observed by the four spacecraft. Before crossing the $N = 0$ current sheet, the traces are blue indicating the angle is close to zero. After the crossing, the traces become white or light red, indicating the angle now becomes almost $90° \sim 100°$. The sketch of Figure 7(b) illustrates this feature by showing the reconnection picture in the $L-M$ plane. $\boldsymbol{B_1}$ represents the field lines before the current sheet crossing (at $-N$) and $\boldsymbol{B_2}$ represents the field lines after the current sheet crossing (at $+N$). The stars highlight the

reconnection sites which follow $\boldsymbol{B_1}$. We point out, however, that the x-line could also have aligned with B_2 unless there is an asymmetry. Clearly, the governing force of a nonorthogonal x-line requires further investigation.

6. Summary

To summarize, this paper reports a second event observed by MMS where the x-line is not perpendicular to the reconnection plane, evidenced by (1) the fast motion in L suggested by the field measurement while there is a small ion velocity in L; and (2) the minimum directional derivative direction deviates from the M direction by $\sim 40°$. The discovery of a second similar event is to support the generality of such phenomenon even though it may seem peculiar in the beginning as it contrasts the classic reconnection picture where the x-line is orthogonal to the reconnection plane. However, to the best of our knowledge, there is no conclusive theoretical analysis that suggests the x-line must spread in an orthogonal direction. The fact that there is more than one event with this signature extends our current understanding of magnetic reconnection and opens up more questions to be discussed regarding the three-dimensional picture of reconnection. Another important finding is that, even though the x-line is nonorthogonal, reconnection can remain quasi-2D. The $L-N$ plane well behaved as expected from a textbook 2D reconnection event. This suggests that the x-line direction has little impact on the in-plane behaviors. Because the direction of the x-line links the microphysics of the EDR to the large-scale behavior of magnetic reconnection, these observations call for more theoretical and observational studies of magnetic reconnection with a nonorthogonal x-line not only in Earth's magnetotail, but also in other regions of Earth's magnetosphere, in the solar wind, the Sun's corona or even other planet's magnetosphere.

Acknowledgments

We appreciate the efforts of the entire MMS team, including many individuals in spacecraft operation and data acquisition. This research was supported by NASA MMS mission No. NNG04EB99C and NSF award No. AGS-2000222.

ORCID iDs

Yi Qi https://orcid.org/0000-0002-0959-3450
Robert Ergun https://orcid.org/0000-0002-3096-8579
Neha Pathak https://orcid.org/0000-0001-5567-8183
Tak Chu Li https://orcid.org/0000-0002-6367-1886
Stefan Eriksson https://orcid.org/0000-0002-5619-1577
Alexandros Chasapis https://orcid.org/0000-0001-8478-5797
Tien Vo https://orcid.org/0000-0002-8335-1441
David Newman https://orcid.org/0000-0003-0810-1204
Maria Usanova https://orcid.org/0000-0002-0406-6387

References

Arencibia, M., Cassak, P. A., Shay, M. A., & Priest, E. R. 2021, PhPl, 28, 082104
Burch, J. L., Ergun, R. E., Cassak, P. A., et al. 2018, GeoRL, 45, 1237
Burch, J. L., Torbert, R. B., Phan, T. D., et al. 2016, Sci, 352, aaf2939
Cassak, P. A., & Shay, M. A. 2007, PhPl, 14, 102114
Chen, L., Hesse, M., Wang, S., Bessho, N., & Daughton, W. 2016, GeoRL, 43, 2405
Chen, L.-J., Bessho, N., Lefebvre, B., et al. 2008, JGRA, 113, A12213
Dahlin, J. T., Drake, J. F., & Swisdak, M. 2014, PhPl, 21, 092304
Denton, R. E., Sonnerup, B. U. Ö., Russell, C. T., et al. 2018, JGRA, 123, 2274
Drake, J. F., Shay, M. A., & Swisdak, M. 2008, PhPl, 15, 042306
Dungey, J. W. 1961, PhRvL, 6, 47
Dunlop, M. W., Southwood, D. J., Glassmeier, K.-H., & Neubauer, F. M. 1988, AdSpR, 8, 273
Ergun, R. E., Ahmadi, N., Kromyda, L., et al. 2020, ApJ, 898, 153
Ergun, R. E., Chen, L.-J., Wilder, F. D., et al. 2017, GeoRL, 44, 2978
Ergun, R. E., Pathak, N., Usanova, M. E., et al. 2022, ApJL, 935, L8
Ergun, R. E., Tucker, S., Westfall, J., et al. 2016, SSRv, 199, 167
Eriksson, E., Vaivads, A., Graham, D. B., et al. 2018, GeoRL, 45, 8081
Fargette, N., Lavraud, B., Øieroset, M., et al. 2020, GeoRL, 47, e86726
Fu, H. S., Cao, J. B., Cao, D., et al. 2019, GeoRL, 46, 48
Fujimoto, K., & Cao, J. 2021, GeoRL, 48, e94431
Fuselier, S. A., Webster, J. M., Trattner, K. J., et al. 2021, JGRA, 126, e29789
Genestreti, K. J., Li, X., Liu, Y.-H., et al. 2022, PhPl, 29, 082107
Genestreti, K. J., Liu, Y.-H., Phan, T.-D., et al. 2020, JGRA, 125, e27985
Genestreti, K. J., Nakamura, T. K. M., Nakamura, R., et al. 2018, JGRA, 123, 9130
Gingell, I., Schwartz, S. J., Eastwood, J. P., et al. 2019, GeoRL, 46, 1177
Gonzalez, W. D., Parker, E. N., Mozer, F. S., et al. 2016, Magnetic Reconnection, Vol. 427 (Berlin: Springer), 1
Gosling, J. T., Skoug, R. M., McComas, D. J., & Smith, C. W. 2005, JGRA, 110, A01107
Graham, D. B., Khotyaintsev, Yu. V., Norgren, C., et al. 2016, GeoRL, 43, 4691
Graham, D. B., Khotyaintsev, Yu. V., Norgren, C., et al. 2019, JGRA, 124, 8727
Hasegawa, H., Denton, R. E., Nakamura, T. K. M., et al. 2022, JGRA, 127, e30408
Hesse, M., Aunai, N., Zenitani, S., Kuznetsova, M., & Birn, J. 2013, PhPl, 20, 061210
Hesse, M., & Cassak, P. A. 2020, JGRA, 125, e25935
Huba, J. D., & Rudakov, L. I. 2002, PhPl, 9, 4435
Hubbert, M., Qi, Y., Russell, C. T., et al. 2021, GeoRL, 48, e91364
Jia, Y., Qi, Y., Lu, S., & Russell, C. T. 2021, JGRA, 126, e28698
Kan, J. R. 1988, JGR, 93, 5613
Li, T. C., Liu, Y., Hesse, M., & Zou, Y. 2020, JGRA, 125, e27094
Li, T. C., Liu, Y.-H., & Qi, Y. 2021, ApJL, 909, L28
Li, T. C., Liu, Y.-H., Qi, Y., et al. 2023, PhRvL, submitted (arXiv:2303.08642)
Lindqvist, P.-A., Olsson, G., Torbert, R. B., et al. 2016, SSRv, 199, 137
Liu, Y., Hesse, M., & Kuznetsova, M. 2015, JGRA, 120, 7331
Liu, Y., Hesse, M., Li, T. C., Kuznetsova, M., & Le, A. 2018, JGRA, 123, 4908
Lu, S., Wang, R., Lu, Q., et al. 2020, NatCo, 11, 5049
Ng, J., Chen, L.-J., Bessho, N., et al. 2022, GeoRL, 49, e99544
Øieroset, M., Phan, T. D., Drake, J. F., et al. 2019, GeoRL, 46, 1937
Parker, E. N. 1957, JGR, 62, 509
Paschmann, G., Øieroset, M., & Phan, T. 2013, SSRv, 178, 385
Pathak, N., Ergun, R. E., Qi, Y., et al. 2022, ApJL, 941, L34
Phan, T. D., Bale, S. D., Eastwood, J. P., et al. 2020, ApJS, 246, 34
Phan, T. D., Eastwood, J. P., Shay, M. A., et al. 2018, Natur, 557, 202
Phan, T. D., Freeman, M. P., Kistler, L. M., et al. 2001, EP&S, 53, 619
Pollock, C., Moore, T., Jacques, A., et al. 2016, SSRv, 199, 331
Pritchard, K. R., Burch, J. L., Fuselier, S. A., et al. 2019, GeoRL, 46, 10274
Qi, Y., Li, T. C., Russell, C. T., et al. 2022, ApJL, 926, L34
Qi, Y., Russell, C. T., Jia, Y., & Hubbert, M. 2020, GeoRL, 47, e90314
Retinò, A., Sundkvist, D., Vaivads, A., et al. 2007, NatPh, 3, 235
Rogers, A. J., Farrugia, C. J., & Torbert, R. B. 2019, JGRA, 124, 6487
Russell, C. T., Anderson, B. J., Baumjohann, W., et al. 2016, SSRv, 199, 189
Russell, C. T., & Qi, Y. 2020, GeoRL, 47, e87620
Russell, C. T., Strangeway, R. J., Zhao, C., et al. 2017, Sci, 356, 960
Schreier, R., Swisdak, M., Drake, J. F., & Cassak, P. A. 2010, PhPl, 17, 110704
Shepherd, L. S., & Cassak, P. A. 2012, JGRA, 117, A10101
Shi, Q. Q., Shen, C., Pu, Z. Y., et al. 2005, GeoRL, 32, L12105
Shi, Q. Q., Tian, A. M., Bai, S. C., et al. 2019, SSRv, 215, 35
Smartt, R. N., Zhang, Z., & Smutko, M. F. 1993, SoPh, 148, 139
Swisdak, M., & Drake, J. F. 2007, GeoRL, 34, L11106
Torbert, R. B., Burch, J. L., Phan, T. D., et al. 2018, Sci, 362, 1391
Torbert, R. B., Russell, C. T., Magnes, W., et al. 2016, SSRv, 199, 105
Wang, S., Chen, L., Bessho, N., et al. 2019, GeoRL, 46, 562
Wang, S., Chen, L., Bessho, N., et al. 2022, JGRA, 127, e30109
Webster, J. M., Burch, J. L., Reiff, P. H., et al. 2018, JGRA, 123, 4858
Xue, Z., Yan, X., Cheng, X., et al. 2016, NatCo, 7, 11837
Zhou, M., Deng, X. H., Zhong, Z. H., et al. 2019, ApJ, 870, 34
Zou, Y., Walsh, B. M., Nishimura, Y., et al. 2019, AnGeo, 37, 215